Hindawi
Structural Control and Health Monitoring
Volume 2023, Article ID 3203261, 19 pages
https://doi.org/10.1155/2023/3203261

*Research Article*

# Reference Point-Free Measurement of Bridge Dynamic Deflection by Fusing Hydraulic Leveling and Accelerometer Signals

**Zhibin Jin**,[1] **Hongda Xia**,[1] **Wenbo Ni**,[2] **and Haoyuan Yang**[1]

[1]*Department of Bridge Engineering, Southwest Jiaotong University, Chengdu 610031, China*
[2]*School of Mechanical Engineering, Southwest Jiaotong University, Chengdu 610031, China*

Correspondence should be addressed to Hongda Xia; hongda.xia@my.swjtu.edu.cn

Received 8 November 2022; Revised 9 January 2023; Accepted 11 January 2023; Published 9 February 2023

Academic Editor: Yong Xia



Structural health monitoring (SHM) is widely applied to assess the service condition of bridges. Deflection measurements are essential to determine a bridge's performance, and in particular, dynamic deflection is increasingly required in SHM. However, continuous and high-precision measurements of the absolute dynamic deflection are challenging without a reference point placed at a distance from the bridge. We proposed a reference point-free dynamic deflection measurement system consisting of a level sensor and an accelerometer. The level sensor measures the low-frequency deflection components, while the accelerometer measures the high-frequency deflection components. We redesigned the level sensor from the hydrostatic level sensor and further provided a correction method to achieve the dynamic deflection measurement. A numerical algorithm fuses the signals from the level sensor and accelerometer to obtain the absolute dynamic deflection, and key parameters are calculated. The accuracy of the measurement system was tested in the laboratory, and the sensor results were similar to the ones obtained by the laser test under simple harmonic and random excitations. Field tests conducted on a T-shaped rigid frame bridge with random traffic flow indicate that the system can achieve continuous high-precision deflection measurements of bridges loaded by traffic flow.

## 1. Introduction

Bridge deflection measurements are crucial for operational safety and structural damage assessment, as they are highly indicative of the bridge performance. Therefore, both static and dynamic deflection measurements have become an increasingly indispensable part of structural health monitoring (SHM).

Static deflection is mostly measured by global positioning systems (GPSs), total station, and hydrostatic leveling systems (HLSs) [1–4] in static load testing and long-term deformation monitoring. These commercial instruments can achieve stable and accurate static deflection measurements, albeit only at certain structure points. The points deflection measurement is often unsatisfactory, and the inclinometer is often employed to reconstruct the static deflection curve of the entire bridge [5, 6].

Dynamic deflection is, to some extent, more important than static deflection, because it reflects the bridge stiffness variation and dynamic properties, which are essential for assessing its real-time service condition. Dynamic deflection measurement techniques are sorted according to whether a ground reference point at a distance from the bridge is required.

Dynamic deflection measurements with reference points, such as the ground-based interferometric radar, total stations, laser technology, and linear variable differential transformers (LVDTs), are demonstrated measurement methods. The image by the interferometric survey (IBIS-S) system is a ground-based interferometric radar displacement measuring instrument. Therein, the radar transmitter is located at a fixed position on the ground at a distance away from bridges, serving as the reference point. The system can achieve an accuracy of 0.1 mm in the dynamic mode with a sampling frequency of up to 200 Hz [7–9]. Marendić et al.

used a robotic total station fixed at a distance from the bridge to measure its deflection with the accuracy of ±2.2 mm at 20 Hz sampling frequency [10]. Zhang et al. [11] achieved 0.2 mm dynamic deflection measurement accuracy based on laser projection and image processing technology. Linear variable differential transformers (LVDTs) have higher measurement accuracy, albeit they are more difficult to install [12]. Recently, vision-based methods have been introduced to measure bridge deformation, most requiring a fixed camera near the bridge. The measurement accuracy of these methods ranges from 0.01 to 1 mm [13–16]. The vision-based system sampling frequency is related to the camera performance, most frequencies being around 60 Hz.

Systems with ground reference points exhibit high measurement accuracy (Table 1); however, as bridges may span rivers, villages, or other roads, it is not an easy task to establish a fixed reference point outside the bridge. Therefore, there is a demand for reference point-free dynamic deflection measurement.

The positioning system using satellites does not require a ground reference point, but the accuracy for dynamic measurement only achieves 1 cm [17]. Yoon et al. [18] used an unmanned aerial system to measure the absolute displacement of bridges, whose RMSE is 2.14 mm. Liu et al. [19] employed the connected pipe system (CPS) to monitor the deflection of a long-span suspension bridge. The CPS measures the dynamic deflection of the bridge caused by slowly passing heavy vehicles, whereas the small deflection caused by lighter and faster vehicles cannot be measured accurately. Estimating the displacement using only acceleration data likewise satisfies the requirement of no ground reference point, as the theoretical displacement can be obtained by integrating the acceleration signal twice. However, this method is plagued by drift over time, and several researchers attempted to overcome this problem. Arias-Lara and De-la-Colina [20] compared seven correction algorithms to solve the displacement drift problem, where each algorithm can only be used under specific prerequisites. Converse and Gerald Brady [21] and Chiu [22] corrected the recorded acceleration by baseline correction to reconstruct the displacement. This method was first used in earthquake engineering. The algorithm includes three steps: (1) fitting the baseline of acceleration by the least squares, (2) designing a high-pass filter for acceleration, and (3) decreasing the initial values in velocity on the first integration result. Park et al. [23] used acceleration to estimate the bridge deflection under the moving vehicle load; in this method, the displacement is easily calculated if the initial velocity is known under the zero initial displacement condition. However, the bridge's zero initial displacement condition is difficult to determine under actual constant traffic flow, limiting the method in continuous measurement. Liu et al. used a sensing system composed of one passive servo electromagnetic induction (PSEMI) velocity sensor and one built-in hardware integrator unit. The measurement errors are less than 10% compared to LVDT [24].

Achieving reference point-free dynamic displacement measurements with a single sensor remains a challenge, and fusion methods have been employed as a solution. Ozdagli et al. [25] used tilt and acceleration to obtain displacement. Xu et al. [26] fused the GPS and accelerometer to improve the long-span bridge's deflection measurement accuracy using a multirate Kalman filter. The modal frequency was determined to be 0.63 Hz; however, the dynamic recognition frequency proved too low for small-span bridges. Cho et al. [27] and Sarwar and Park [28] proposed an accurate displacement estimation method by optimally utilizing acceleration and strain for simply supported bridges. The method requires a definite proportional connection between the strain and deflection at the same location on a bridge, making it not suitable for measuring deflections on bridges without the abovementioned relationship, such as cable-supported bridges.

Table 1 lists the dynamic deflection measurement methods, including whether a ground reference point at a distance from the bridge is required, the applicable bridge type, the highest sampling rates, and the obtained accuracy.

Long-span cable-supported or small-span simply supported bridges have applicable reference point-free methods for deflection measurements. This study focuses on small-span or midspan bridges with a maximum deflection of several millimeters or centimeters. We proposed a reference point-free continuous bridge dynamic deflection measurement system comprising a leveling system and accelerometer using the sensor fusion method. The system includes fixed and moving ends. The fixed end is placed on the pier top as the reference point, while the moving end is placed at the measurement point. Only the relative displacement between both ends by the total station on the bridge is necessary to attain continuous dynamic deflection monitoring without ground reference points. The fundamental contribution of the proposed method is shown in Figure 1.

The rest of this paper is organized as follows. Section 2 introduces the correction method of the hydrostatic leveling systems (HLS) employed for dynamic displacement measurement and further details its design. Section 3 presents the algorithm that fuses the leveling and acceleration signals to reconstruct the displacement. We employed this algorithm to fuse a liquid-level sensor and accelerometer for displacement measurement for the first time. Sections 4 and 5 demonstrate the performance of the measuring system in laboratory and field tests.

## 2. Theory and Techniques for Dynamic Hydraulic Leveling System (DHLS)

The theory behind the correction algorithm for the DHLS is introduced herein based on its dynamic characteristics, and the leveling identification method, based on image recognition, is introduced. The design concerns of the DHLS are addressed, and the design is based on the full-field HLS.

*2.1. Composition of Leveling System and Fluid's Forced Oscillation.* The system consists of two water containers connected by a communicating pipe at the base. The distance

Table 1: Comparison of deflection measurement methods.

| Method | Ground reference point | Applicable bridge type | Highest sampling rates (Hz) | Accuracy |
|---|---|---|---|---|
| Total station | Yes | Small-span bridges | 20 | ~2 mm |
| GPS-RTK | Yes | Any | 100 | ~1-2 mm |
| Interferometric radar technology (IBIS) | Yes | Any | 200 | 0.1 mm |
| Vision-based | Yes | Any | 60 | ~1 mm |
| *Acceleration estimation | No | Small-span bridges | 500 | <1 mm |
| Acceleration-GPS fusion | No | Mostly long-span bridges | 20 | ~1 cm |
| *Acceleration-strain fusion | No | Small-span bridges (simply supported) | 500 | <1 mm |

Methods with *have other limitations that are not convenient to list in the table, whose details are presented in the introduction.

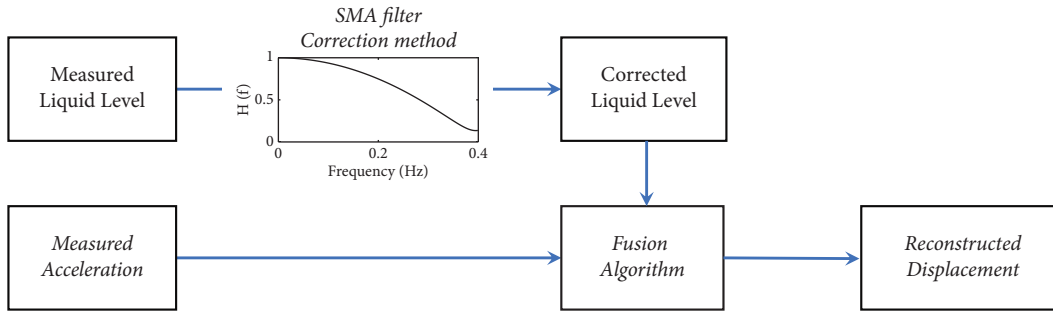


Figure 1: The fundamental contribution of the proposed method.

between the two containers is $L$, and the communicating pipe diameter is $d = 2r$. Air tubes are installed on containers to prevent foreign objects from falling into them, while ensuring the connection between the fluid and the atmosphere. Because of the principle of communicating vessels, the liquid level in the container tends to maintain the same height at the equilibrium position. The schematic diagram of the system is shown in Figure 2.

The free oscillation equation has been previously derived in numerous studies, such as [29]. In this section, we derive the forced oscillation equation.

In Figure 2, the container at the middle of the span moves $y(t)$ relative to the other. Consequently, the liquid in the pipe starts to flow. To obtain the flow state, we take a liquid microelement d$l$ in the pipe for analysis, as shown in Figure 2. For both sides of this microelement, the force difference is given as follows:

$$\begin{aligned}\Delta F_p &= F_l - F_r \\ &= p(l,t)\alpha_p - \left(p(l,t) + \frac{\partial p(l,t)}{\partial l}\mathrm{d}l\right)\alpha_p,\end{aligned} \tag{1}$$

where $p(l,t)$ and $p(l,t) + \partial p(l,t)/\partial l \mathrm{d}l$ are pressure on both surfaces of the microelement and $\alpha_p$ is the cross-sectional area of the connecting pipe.

According to Poiseuille's Law, the viscous resistance is described as follows:

$$F_c = -\frac{8\mu v(t)\alpha_p \cdot \mathrm{d}l}{r^2}, \tag{2}$$

where $v(t)$ is the average velocity of profile flow in the connecting pipe and $\mu$ is the coefficient of viscosity of the fluid.

The mass $m$ of the microelement is given as follows:

$$m = \rho\alpha_p \cdot \mathrm{d}l. \tag{3}$$

The component of gravity force along the bottom pipe is $mg\sin\theta$.

$$\mathrm{mg}\sin\theta = \rho\alpha_p g \cdot \mathrm{d}l\frac{\partial y(t)}{\partial l}, \tag{4}$$

where $\rho$ is the density of the liquid in the pipe, $g$ is the gravitational acceleration, and $\theta$ is the angle between the pipe and the horizontal plane. It can be assumed that $\sin\theta = \partial y(t)/\partial l$ when $\theta$ is very small.

The inertial force $F_I$ of the microelement is given by the following formula:

$$\begin{aligned}F_I &= -\mathrm{ma} \\ &= -\rho\alpha_p \cdot \mathrm{d}l\frac{\mathrm{d}v(t)}{dt}.\end{aligned} \tag{5}$$

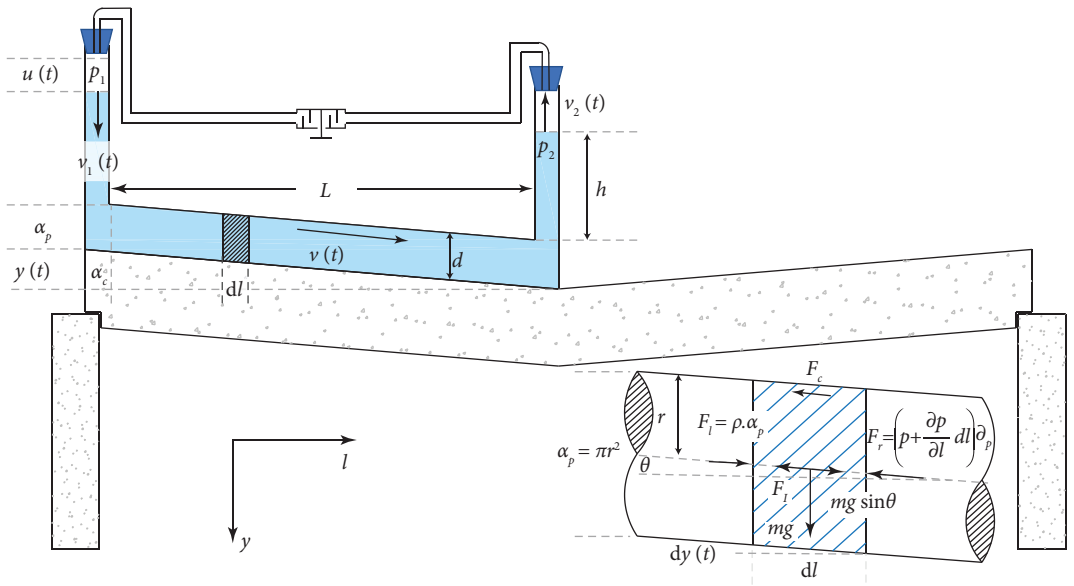


Figure 2: Schematic diagram for the derivation of forced oscillation of fluid in the pipe.

According to Newton's second law, the force-balance condition of the microelement can be written as follows:

$$\left[p(l,t)\alpha_p - \left(p(l,t) + \frac{\partial p(l,t)}{\partial l}\mathrm{d}l\right)\alpha_p\right] - \frac{8\mu v(t)\alpha_p \cdot \mathrm{d}l}{r^2} + \rho\alpha_p g \cdot \mathrm{d}l\frac{\partial y(t)}{\partial l} - \rho\alpha_p \cdot \mathrm{d}l\frac{\mathrm{d}v(t)}{\mathrm{d}t} = 0. \tag{6}$$

By integrating equation (6) along the $x$-axis from the left to the right ends of the pipe, the following equation is obtained:

$$-\rho g\alpha_p \cdot 2u(t) - \frac{8\mu v(t)\alpha_p \cdot L}{r^2} + \rho g\alpha_p \cdot y(t) - \rho\alpha_p L \cdot \frac{\mathrm{d}v(t)}{\mathrm{d}t} = 0, \tag{7}$$

where $u(t)$ is the vertical position of liquid level relative to the container.

Simultaneously, we know that in the containers, the pressure is equal at both liquid surfaces, $p_1 = p_2$. The average velocity of flow in both the containers is $v_1(t) = \mathrm{d}u/\mathrm{d}t = v_2(t)$ and $v(t) = (\alpha_c/\alpha_p)v_1(t)$, where $\alpha_c$ is the cross-sectional area of the liquid container. Substituting the above conditions, the following equation is obtained:

$$-2u - \frac{8\mu v_1 L}{\rho g\pi r^4} \cdot \frac{\alpha_c}{\alpha_p} - \frac{\sigma}{g} \cdot \frac{\mathrm{d}v_1}{\mathrm{d}t} + y = 0, \tag{8}$$

where $\sigma = 2h + (\alpha_c/\alpha_p)L \approx (\alpha_c/\alpha_p)L$ (because $2h \ll L$) and $h$ is the height of the liquid level of the container at equilibrium condition.

To simplify equation (8), we move the terms containing excitation $y(t)$ and response $u(t)$ to each side of the equation as follows:

$$\frac{\mathrm{d}^2u(t)}{\mathrm{d}t^2} + \frac{8\mu}{\rho r^2}\frac{\mathrm{d}u(t)}{\mathrm{d}t} + \frac{2g}{\sigma}u(t) = \frac{g}{\sigma}y(t). \tag{9}$$

Rewriting equation (9) into a standard form composed of $\omega_n$ and $\xi$ as follows:

$$\frac{\mathrm{d}^2u(t)}{\mathrm{d}t^2} + 2\xi\omega_n\frac{\mathrm{d}u(t)}{\mathrm{d}t} + \omega_n^2 u(t) = \frac{g}{\sigma}y(t), \tag{10}$$

where the natural frequency is $\omega_n = \sqrt{2g/(2h + L\alpha_c/\alpha_p)}$ and the damping ratio is $\zeta = \sqrt{8\mu^2\pi^2 L\alpha_c/\rho^2 g{\alpha_p}^3}$

*2.2. Liquid Level Identification Method Based on Image Recognition.* The desired dynamic displacement is obtained by correcting the liquid-level change. To obtain direct leveling changes, we completed the liquid-level recognition system (LRS), which uses image recognition technologies

with the help of Liu et al. [30] The LRS comprises a camera, shade panel, LED light source, and communicating pipe. The image recognition process is assisted by OpenCV, which provides a real-time optimized computer vision library, tools, and hardware. The image recognition process is illustrated in Figure 3. Its tasks include (1) converting the original color image to grayscale and capturing its target area, (2) performing bilateral filtering on the image to remove noise while protecting the edge information of the image, (3) binarizing the liquid-level edge and background by threshold segmentation and getting the segmented image, (4) extracting the complete edge contour of the liquid level using the Canny edge detection algorithm in OpenCV, and (5) using subpixel edge detection methods to improve the accuracy of the liquid-level edge recognition. We obtain the liquid-level bottom coordinates $C_{\text{pixel}}(x_h, y_v)$ of the subpixel edge image by the five steps described above.

We used the device shown in Figure 4(a) to scale the vertical pixel coordinates $y_v$ (given by the image recognition system) to the reality displacement (measured by the laser displacement meter). The relationship between $k$ and $y_v$ is shown in the following formula; $\widehat{\beta}_0$ and $\widehat{\beta}_1$ can be obtained by multiple tests.

$$k = \widehat{\beta}_0 + \widehat{\beta}_1 y_v, \tag{11}$$

where $\widehat{\beta}_0 = \sum_{i=1}^{n} y_{vi}^2 \sum_{i=1}^{n} k_i - \sum_{i=1}^{n} y_{vi} \sum_{i=1}^{n} k_i y_{vi} / n \sum_{i=1}^{n} y_{vi}^2 - (\sum_{i=1}^{n} k_i)^2$ and $\widehat{\beta}_1 = n \sum_{i=1}^{n} y_{vi} k_i - \sum_{i=1}^{n} y_{vi} \sum_{i=1}^{n} k_i / n \sum_{i=1}^{n} y_{vi}^2 - (\sum_{i=1}^{n} k_i)^2$, $k_i$ and $y_{vi}$ are the result data of each test and $n$ is the total number of tests.

Furthermore, the natural frequency of the liquid level in the DHLS is designed as 0.4 Hz. The damping ratio is 0.068, which filters out high-frequency components. The camera's sampling frequency is ~25 Hz. Thus, half of the sampling frequency is ~12.5 Hz, which is significantly higher than the signal frequency of 0.397 Hz, and thus meets the requirements of Nyquist law.

*2.3. Correction Method for DHLS.* The amplitude-frequency characteristic $|D(\omega)|$ of the DHLS is given as follows:

$$\begin{aligned} |D(\omega)| &= \frac{|U(\omega)|}{|Y(\omega)|} \\ &= \frac{1}{\sqrt{\left(1-\beta^2\right)^2 + (2\xi\beta)^2}}, \end{aligned} \tag{12}$$

where $|Y(\omega)|$ is maximum amplitudes of the liquid container's displacement and $|U(\omega)|$ is twice of fluid level measured by DHLS under harmonic excitation with different frequencies. Only the amplitude-frequency characteristic is considered, and the effect of phase difference is ignored. $\beta = \omega/\omega_n$, where $\omega_n$ is the natural frequency of HLS and $\omega$ is excitation frequency.

Suppose we can design a filter whose transfer function is $1/|D(\omega)|$ and which can reconstruct the bridge deflection $|Y(\omega)|$ from the measured liquid-level difference $|U(\omega)|$, as shown in the following equation:

$$|Y(\omega)| = |U(\omega)| \cdot \frac{1}{|D(\omega)|}. \tag{13}$$

The simple moving average (SMA) filter is computationally effective in the time domain. Here, the filter function $1/|D(\omega)|$ is approximated by the moving average method. Assuming the window length of the moving average filter is $2t_m$, its pulse-response function in the time domain reads as follows [31]:

$$H(t) = \begin{cases} \dfrac{1}{2t_m}, & (-t_m, t_m), \\ 0, & \text{esel.} \end{cases} \tag{14}$$

The response function in the frequency domain is the fourier transform (FT) of its pulse-response function in the time domain. Thus, the frequency response function $H(\omega)$ of the moving average method is as follows:

$$\begin{aligned} H(\omega) &= \int_{-t_m}^{t_m} H(t) e^{j\omega t} dt \\ &= \frac{\sin(\omega t_m)}{\omega t_m} \approx \frac{\omega t_m}{\omega t_m} - \frac{(\omega t_m)^3}{6\omega t_m}, \end{aligned} \tag{15}$$

where $\sin \omega t$ is turned into the Taylor Expansion to facilitate the derivation, in the last expression of equation (15).

To obtain the optimal $t_m$ make $H(\omega)$ appropriate $1/|D(\omega)|$. We construct the following function equation (15), which minimizes the square difference between the frequency response function of SMA ($H(\omega)$) and HLS $1/|D(\omega)|$. In the last expression of equation (15), $\omega$ is discretized into frequency points $\omega = \omega_{(i)} i = 1, 2, \ldots, n$.

$$\begin{aligned} J(t_m) &= \min_{t_m} \left\| H(\omega) - \frac{1}{|D(\omega)|} \right\|_2^2 \\ &= \min_{t_m} \sum_{i=1}^{n} \left\{ \left[ \frac{\omega_{(i)} t_m}{\omega_{(i)} t_m} - \frac{(\omega_{(i)} t_m)^3}{6\omega_{(i)} t_m} \right] - \sqrt{\left(1 - \frac{\omega_{(i)}^2}{\omega_n^2}\right)^2 + \left(2\xi \frac{\omega_{(i)}}{\omega_n}\right)^2} \right\}^2. \end{aligned} \tag{16}$$

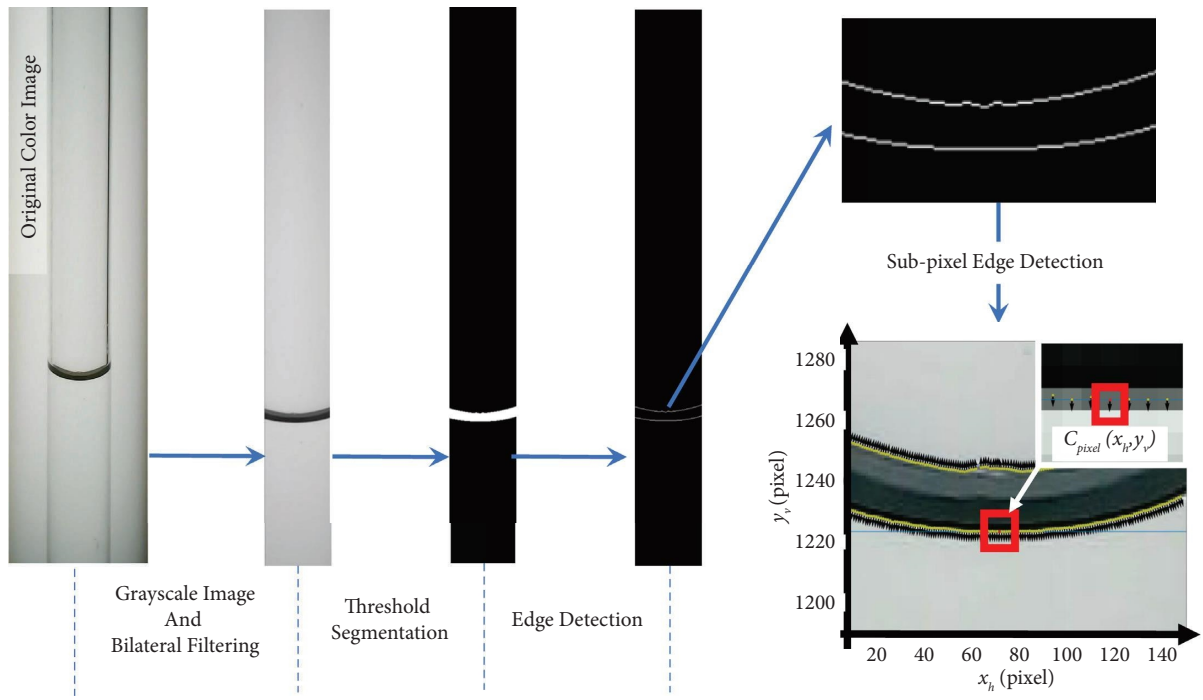


FIGURE 3: The process of obtaining subpixel bottom edge coordinates of the liquid level.

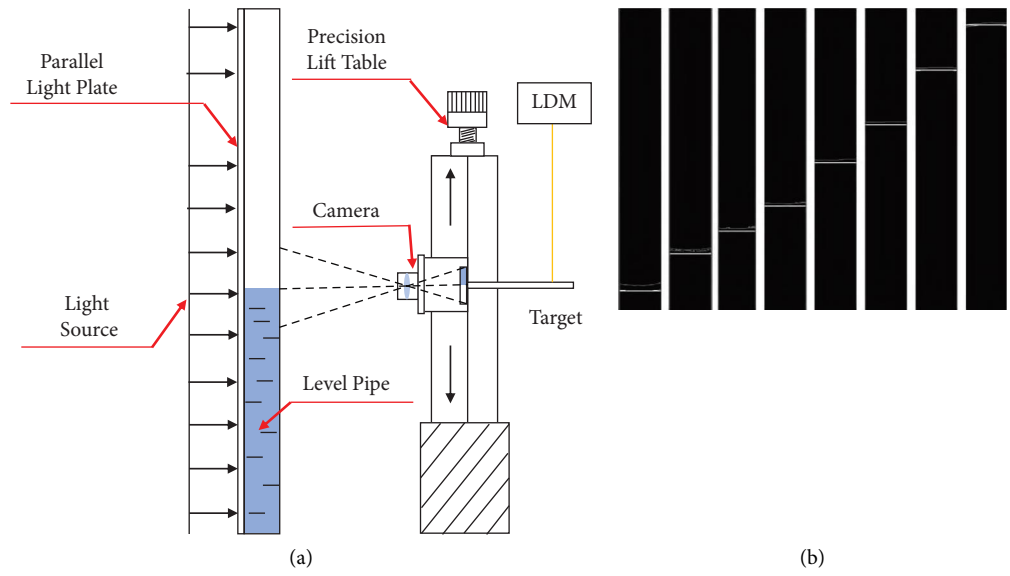


FIGURE 4: Device for liquid-level calibration to displacement (a) drawing for the test device and (b) the location of the lowest line of the concave surface at different liquid levels.

In equation (16), $\|f(*)\|_2^2$ denotes the square of the 2-Norm (square root of the integral of $f(*)$ squared over the interval). Then, equation (16) simplifies as follows:

$$J(t_m) = \min_{t_m} \sum_{i=1}^{n} \left\{ -\frac{\omega_{(i)}^2}{6} t_m^2 - \left[ \sqrt{\left(1 - \frac{\omega_{(i)}^2}{\omega_n^2}\right)^2 + \left(2\xi \frac{\omega_{(i)}}{\omega_n}\right)^2} + 1 \right] \right\}^2. \tag{17}$$

Equation (17) is expanded into matrix form $\omega_{(i)} = n\Delta\omega$ with $n = 1, 2, \ldots, i$ as the discrete interval.

$$J(t_m) = \min_{t_m} \begin{bmatrix} -\frac{\Delta\omega^2}{6} t_m^2 - \left[ \sqrt{\left(1 - \frac{\Delta\omega^2}{\omega_n^2}\right)^2 + \left(2\xi \frac{\Delta\omega}{\omega_n}\right)^2} - 1 \right] \\ -\frac{(2\Delta\omega)^2}{6} t_m^2 - \left[ \sqrt{\left(1 - \frac{(2\Delta\omega)^2}{\omega_n^2}\right)^2 + \left(2\xi \frac{(2\Delta\omega)}{\omega_n}\right)^2} - 1 \right] \\ \vdots \\ -\frac{\omega_n^2}{6} t_m^2 - \left[ \sqrt{\left(1 - \frac{\omega_n^2}{\omega_n^2}\right)^2 + \left(2\xi \frac{\omega_n}{\omega_n}\right)^2} - 1 \right] \end{bmatrix}^T \begin{bmatrix} -\frac{\Delta\omega^2}{6} t_m^2 - \left[ \sqrt{\left(1 - \frac{\Delta\omega^2}{\omega_n^2}\right)^2 + \left(2\xi \frac{\Delta\omega}{\omega_n}\right)^2} - 1 \right] \\ -\frac{(2\Delta\omega)^2}{6} t_m^2 - \left[ \sqrt{\left(1 - \frac{(2\Delta\omega)^2}{\omega_n^2}\right)^2 + \left(2\xi \frac{(2\Delta\omega)}{\omega_n}\right)^2} - 1 \right] \\ \vdots \\ -\frac{\omega_n^2}{6} t_m^2 - \left[ \sqrt{\left(1 - \frac{\omega_n^2}{\omega_n^2}\right)^2 + \left(2\xi \frac{\omega_n}{\omega_n}\right)^2} - 1 \right] \end{bmatrix}. \tag{18}$$

Let $x^{(\omega_i)} = -\omega_{(i)}^2/6, X = [x^{(\omega_1)}, x^{(\omega_2)} \ldots x^{(\omega_i)}]^T$ and $g^{(\omega_i)} = \sqrt{(1 - \omega_{(i)}^2/\omega_n^2)^2 + (2\xi\omega_{(i)}/\omega_n)^2} + 1, G = [g^{(\omega_1)}, g^{(\omega_2)} \ldots g^{(\omega_i)}]^T$. The complex formula in equation (18) is replaced with $x^{(\omega_i)}$ and $g^{(\omega_i)}$, such that

$$\begin{aligned} J(t_m) &= \min_{t_m} \sum_{i=1}^{m} \left( x^{(\omega_i)} \cdot t_m^2 - g^{(\omega_i)} \right)^2 \\ &= \min_{t_m} \left( X t_m^2 - G \right)^T \left( X t_m^2 - G \right). \end{aligned} \tag{19}$$

Finally, the length of the moving average window $2t_m$ is determined by letting the derivative of $(Xt_m^2 - G)^T (Xt_m^2 - G)$ equal to zero.

$$t_m = \sqrt{\left[X^T X\right]^{-1} X^T G}. \tag{20}$$

*2.4. Design Example and Laboratory Test for the DHLS.* The length of the connecting pipe $L$ and the area ratio $\alpha_c/\alpha_p$ are the main factors affecting the measurement performance of DHLS. The length of the connecting pipe is determined by the span of the bridge to be measured. In this design solution, assuming that the bridge span is 30 m, we determined that the length of the connecting pipe is 15 m. The area ratio adjusts the natural frequency of the liquid oscillation after determination of the pipe length (equation (10)). According to the correction in the previous section, the suitable measuring frequency range of DHLS is 0 to $\omega_n$. Meanwhile, the displacement measured by DHLS must be fused with the acceleration. We determine $\omega_n$ by the applicable frequency range of the accelerometer. The microelectro-mechanical system (MEMS) accelerometer selected in this study has a minimum measurement frequency of 0.4 Hz under the premise of ensuring product measurement accuracy. Finally, by substituting $\omega_n = 0.4$ Hz and $L = 15$ m into equation (10), the area ratio $\alpha_c/\alpha_p = 1/4.7$ can be obtained.

We conducted experiments to test the designed DHLS system. The experimental setup includes a shaking table, an LDM, and a liquid-level measurement system, as shown in Figure 5. The device is also used to verify the fusion algorithm in the following section, explaining the installation of the accelerometer.

The data required for this experiment include the amplitude of the liquid-level oscillation in the fixed end and deck displacement of the shaking table at different excitation frequencies. The deck displacement $y$ is measured by LDM, erected vertically above the shaking table. The liquid-level measurement system yields the liquid-level change $u$ at the fixed end. To obtain the amplitude-frequency characteristics $(1/|D(\omega)|)$ of DHLS, we measure the ratio of $|Y(\omega)|$ and

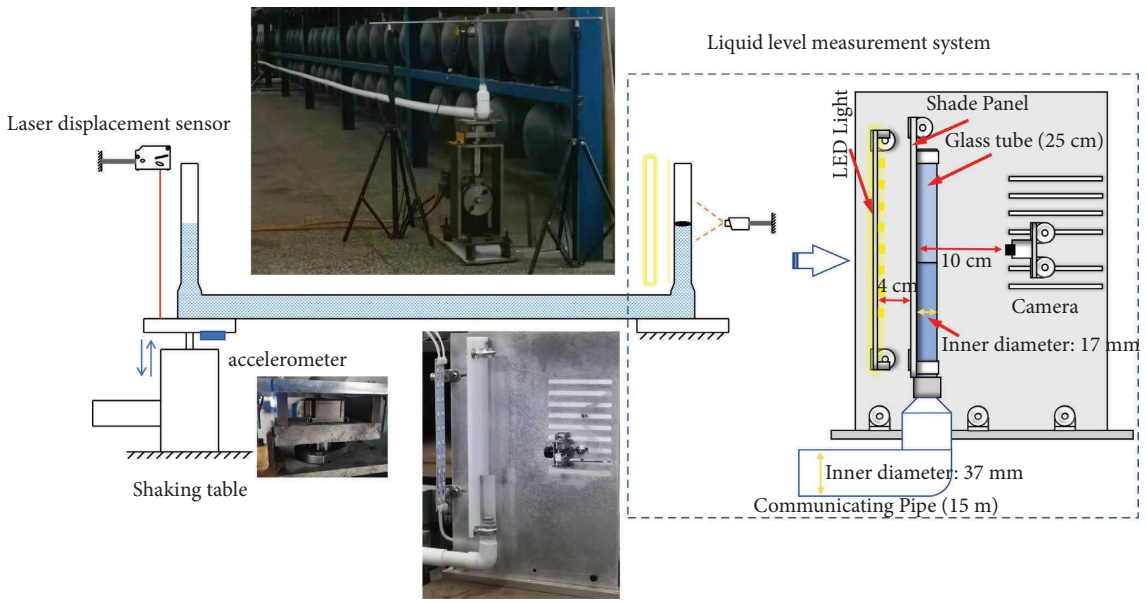


Figure 5: The experimental device of the proposed displacement measurement system.

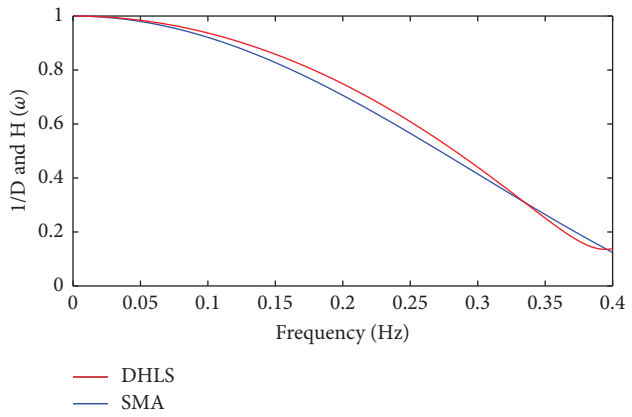


Figure 6: Comparison of amplitude-frequency characteristics of DHLS and SMA.

$|U(\omega)|$ under harmonic excitation at an interval of 0.05 Hz between 0 and 0.4 Hz.

The experimental measurement of $\omega_n$ is 0.397 Hz, which is consistent with the expected result. Then, we identify the frequency response function ($H(\omega)$) of SMA. Figure 6 shows the comparison of measured DHLS amplitude-frequency characteristics and the theoretical value of SMA.

## 3. Fusion Hydraulic Leveling and Accelerometer Signals for Deflection Measurement

Theoretically, the displacement signal is obtained after integrating the acceleration signal twice. Accelerometers are known to have large errors in low-frequency acceleration measurements, and it may produce a drift in the displacement reconstruction. To address this, we apply the corrected hydraulic leveling measurement signal as a supplement to eliminate displacement drift and low-frequency errors from acceleration signals.

Acceleration is the second-order differential of displacement, as indicated in the following formula:

$$a(t) = \frac{d^2u(t)}{dt^2} = \overline{a}(t) + \varepsilon_a, \tag{21}$$

where $a(t)$ is the real acceleration, expressed in terms of displacement through a second-order ordinary differential equation; $u(t)$ is the real displacement; $\overline{a}(t)$ is the measured acceleration; and $\varepsilon_a$ is measurement error.

Displacement is the double integral of acceleration:

$$u(t) = \int\int [\overline{a}(t) + \varepsilon_a]dtdt = \overline{u}(t) + U_0 + V_0 t + \frac{1}{2}\varepsilon_a t^2, \tag{22}$$

where $\overline{u}(t)$ is the displacement obtained by a double integral of measured acceleration and $U_0$, $V_0$, and $\varepsilon_a$ can be considered as the initial displacement, velocity, and acceleration, respectively.

If the initial state is identified, we easily obtain the reconstructed displacement. The following formula is a vector form used to identify the initial state for discrete measured data.

$$\begin{bmatrix} u(t_1) \\ u(t_2) \\ u(t_3) \\ \vdots \\ u(t_n) \end{bmatrix} = \begin{bmatrix} 0 & 0 & 0 & \cdots & 0 \\ 1 & 0 & 0 & \cdots & 0 \\ 2 & 1 & 0 & \cdots & 0 \\ \vdots & \vdots & \vdots & \ddots & 0 \\ n-1 & n-2 & n-3 & \cdots & 1 \end{bmatrix} \begin{bmatrix} 0 \\ \overline{a}(t_1) \\ \overline{a}(t_2) \\ \vdots \\ \overline{a}(t_{n-1}) \end{bmatrix} \cdot \Delta t^2 + U_0 \begin{bmatrix} 1 \\ 1 \\ 1 \\ \vdots \\ 1 \end{bmatrix} + V_0 \begin{bmatrix} 1 \\ 2 \\ 3 \\ \vdots \\ n \end{bmatrix} \Delta t + \frac{1}{2}\varepsilon_a \begin{bmatrix} 1^2 \\ 2^2 \\ 3^2 \\ \vdots \\ n^2 \end{bmatrix} \Delta t^2. \tag{23}$$

The start time of this string of measured data is $t_0$, the sampling interval is $\Delta t$, the total time is $T = n\Delta t$, and the measured acceleration is $\overline{a}(t_i)$.

To obtain $U_0$, $V_0$, and $\varepsilon_a$, we must fuse the corrected displacement ($U_l$) measured by DHLS. Specifically, we subtract $U_l = \left[ u_l(t_1) \;\; u_l(t_2) \;\; u_l(t_3) \;\; \cdots \;\; u_l(t_n) \right]^T$ from equation (23) and obtain the displacement residual $\Delta U$ as follows:

$$\Delta U = \begin{bmatrix} 0 & 0 & 0 & \cdots & 0 \\ 1 & 0 & 0 & \cdots & 0 \\ 2 & 1 & 0 & \cdots & 0 \\ \vdots & \vdots & \vdots & \ddots & 0 \\ n-1 & n-2 & n-3 & \cdots & 1 \end{bmatrix} \begin{bmatrix} 0 \\ \overline{a}(t_1) \\ \overline{a}(t_2) \\ \vdots \\ \overline{a}(t_{n-1}) \end{bmatrix} \cdot \Delta t^2 + U_0 \begin{bmatrix} 1 \\ 1 \\ 1 \\ \vdots \\ 1 \end{bmatrix} + V_0 \Delta t \begin{bmatrix} 1 \\ 2 \\ 3 \\ \vdots \\ n \end{bmatrix} + \frac{1}{2}\varepsilon_a \Delta t^2 \begin{bmatrix} 1^2 \\ 2^2 \\ 3^2 \\ \vdots \\ n^2 \end{bmatrix} - \begin{bmatrix} u_l(t_1) \\ u_l(t_2) \\ u_l(t_3) \\ \vdots \\ u_l(t_n) \end{bmatrix}. \tag{24}$$

By collecting unknown variables, we obtained the following equation:

$$\Delta U = \left\{ \begin{bmatrix} 1 & 0 & 0 & \cdots & 0 \\ 2 & 1 & 0 & \cdots & 0 \\ 3 & 2 & 1 & \cdots & 0 \\ \vdots & \vdots & \vdots & \ddots & 0 \\ n & n-1 & n-2 & \cdots & 1 \end{bmatrix} \begin{bmatrix} 0 \\ \overline{a}(t_1) \\ \overline{a}(t_2) \\ \vdots \\ \overline{a}(t_{n-1}) \end{bmatrix} - U_l \right\} + \begin{bmatrix} 1 & \Delta t & \frac{1}{2}\Delta t^2 \\ 1 & 2\Delta t & \frac{2^2}{2}\Delta t^2 \\ 1 & 3\Delta t & \frac{3^2}{2}\Delta t^2 \\ \vdots & \vdots & \vdots \\ 1 & n\Delta t & \frac{n^2}{2}\Delta t^2 \end{bmatrix} \begin{bmatrix} U_0 \\ V_0 \\ \varepsilon_a \end{bmatrix}. \tag{25}$$

We rewrite the above equation into a simple form as follows:

$$\Delta U = \left[ L\overline{a} - U_l \right] + C\overline{x}, \tag{26}$$

where $L = \begin{bmatrix} 1 & 0 & 0 & \cdots & 0 \\ 2 & 1 & 0 & \cdots & 0 \\ 3 & 2 & 1 & \cdots & 0 \\ \vdots & \vdots & \vdots & \ddots & 0 \\ n & n-1 & n-2 & \cdots & 1 \end{bmatrix}$, $\overline{a} = \begin{bmatrix} 0 \\ \overline{\mathrm{a}}(t_1) \\ \overline{\mathrm{a}}(t_2) \\ \vdots \\ \overline{\mathrm{a}}(t_{n-1}) \end{bmatrix}$, $U_l = \begin{bmatrix} u_l(t_1) \\ u_l(t_2) \\ u_l(t_3) \\ \vdots \\ u_l(t_n) \end{bmatrix}$, and $\mathrm{C} = \begin{bmatrix} 1 & \Delta t & 1/2\Delta t^2 \\ 1 & 2\Delta t & 2^2/2\Delta t^2 \\ 1 & 3\Delta t & 3^2/2\Delta t^2 \\ \vdots & \vdots & \vdots \\ 1 & n\Delta t & n^2/2\Delta t^2 \end{bmatrix}$ are already known, and only the initial state vector $\overline{x} = \begin{bmatrix} U_0 \\ V_0 \\ \varepsilon_a \end{bmatrix}$ is unknown.

The initial state recognition is transformed into parameter optimization by the following formula:

$$\begin{aligned} \operatorname{Min}_{\Delta U} \prod &= \left\| (L\overline{a} - U_l) + C\overline{x} \right\|_2^2 \\ &= \left[ (L\overline{a} - U_l) + C\overline{x} \right]^{\mathrm{T}} \left[ (L\overline{a} - U_l) + C\overline{x} \right]. \end{aligned} \tag{27}$$

To obtain the solution of the unknown initial state vector $\overline{x}$ in equation (27), we let the derivative of $[(L\overline{a}–U_l) + C\overline{x}]^T [(L\overline{a}–U_l) + C\overline{x}]$ equal to zero. Then, $\overline{x}$ can be represented as follows:

$$\begin{aligned} \overline{x} &= \left[ U_0 V_0 \varepsilon_a \right]^T \\ &= \left( C^T C \right)^{-1} \left[ -C^T \left( L\overline{a} - U_l \right) \right]. \end{aligned} \tag{28}$$

Finally, we obtain the reconstruction displacement by substituting the initial state $U_0, V_0, \varepsilon_a$ into equation (23). The proposed displacement reconstruction method is shown in Figure 7.

## 4. Experiments

We reconstructed the displacement by fusing the hydraulic leveling accelerometer signals. To this end, we redesigned the hydraulic leveling system in Section 2 for the dynamic displacement measurement. The experimental test device in this section is the same as shown in Figure 5. To achieve continuous displacement measurement, the system also includes data processing, storage, and wireless transmission parts. The sensors have different sampling frequencies, and data must be synchronized before applying the proposed algorithm for displacement reconstruction. We added a timestamp to each acquired data during the measurement, and the data format of the measured acceleration $\mathrm{acc}(t_{ai})$ and liquid-level $\mathrm{Level}(t_{ai})$ signal is shown as follows:

$$\begin{aligned} \mathrm{acc}\left(t_{ai}\right) &= \begin{bmatrix} t_{a1} & a_1 \\ t_{a2} & a_2 \\ \vdots & \vdots \\ t_{an} & a_n \end{bmatrix}, \\ \mathrm{Level}\left(t_{Li}\right) &= \begin{bmatrix} t_{L1} & L_1 \\ t_{L2} & L_2 \\ \vdots & \vdots \\ t_{Lm} & L_m \end{bmatrix}. \end{aligned} \tag{29}$$

Then, we fit a cubic spline difference function to the liquid level acquisition data. Finally, we inserted the time $t_{ai}$ of the acceleration data $\mathrm{acc}(t_{\mathrm{ai}})$ into the function to obtain the liquid level after the difference as given by equation (30). In this manner, synchronization between both approaches is achieved and adopted.

$$\mathrm{Level}\left(t_{ai}\right) = \begin{bmatrix} t_{a1} & L_1 \\ t_{a2} & L_2 \\ \vdots & \vdots \\ t_{an} & L_n \end{bmatrix}. \tag{30}$$

A series of tests are conducted to verify whether the proposed displacement measurement system and matching algorithm can meet expectations. The experiment separately measures the harmonic, nonharmonic, and impact displacements.

*4.1. Harmonic Excitation.* We test the accuracy of this system under single-frequency harmonic excitation between 0 and 3 Hz. Figure 8 shows the comparison of the proposed system's displacement measuring results with the LDM. The displacement measured by the proposed system is the same as that of the LDM at 0.2, 0.5, 1.0, and 3.0 Hz.

We employed RMSE to assess the measurement accuracy as follows:

$$\mathrm{RMSE} = \sqrt{\frac{\sum_{i=1}^{N} \left( \mathrm{ref}_i - \mathrm{est}_i \right)^2}{N}}, \tag{31}$$

where $\mathrm{ref}_i$ is the data point measured by the LDM and $\mathrm{est}_i$ is the data point measured by the proposed system. Furthermore, we collected several measurements at different frequencies between 0 and 3.0 Hz.

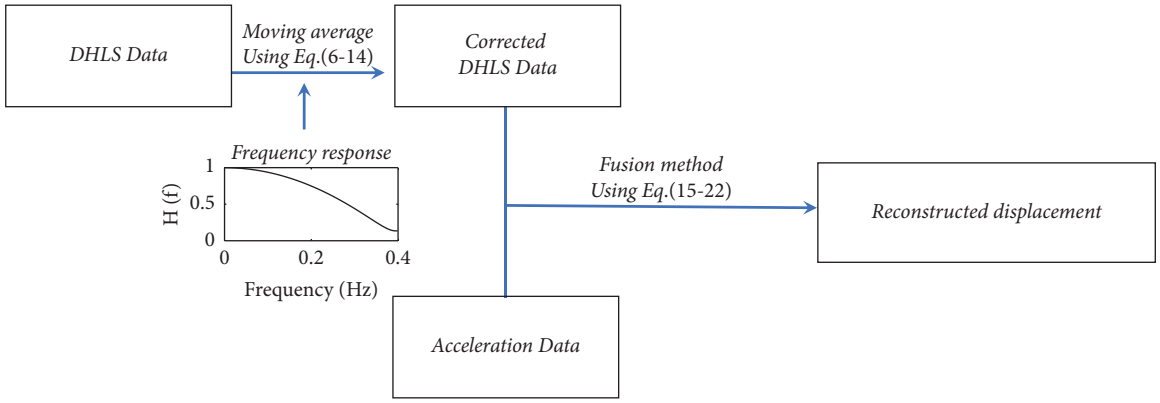


Figure 7: Process of the displacement reconstruction.

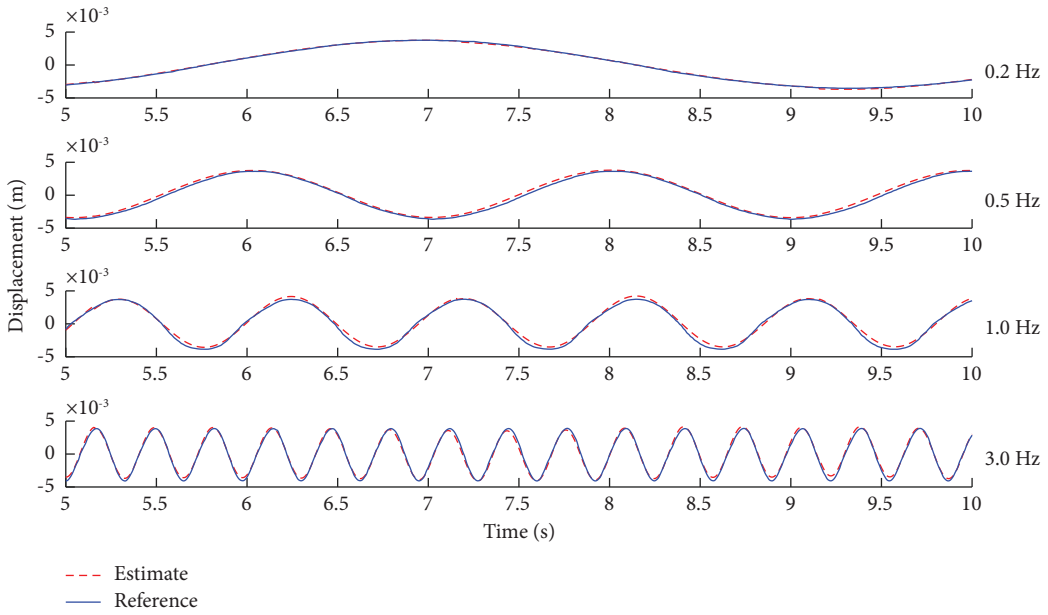


Figure 8: Comparison of displacement measured by the proposed system with LDM (the estimate is the displacement measured by the proposed system and the reference is measured by the LDM).

Figure 9 shows the RMSE of this displacement measurement system at different frequencies. The RSME is below 0.9 mm for all measured frequencies between 0.11 and 3.08 Hz (the frequency interval below 1.0 Hz is 0.1 Hz, between 1.0 and 2.0 Hz is 0.25 Hz, and between 2.0 and 3.0 Hz is 0.5 Hz). We concluded that this measurement system has high accuracy for harmonic displacement excitation.

*4.2. Nonharmonic Excitation.* We test the displacement measurement accuracy under the nonharmonic excitation. According to different frequency concentration ranges, excitations are sorted into four types as shown in Table 2.

Figure 10 shows the displacement measured by the proposed system and LDM when the excitation occurs mainly at low frequencies. In Figure 10, the estimate is the displacement measured by the proposed system, the reference is the displacement measured by the LDM, and the measured results of the LDM are considered as the real displacement (as in Figures 10–13). The frequency components with large amplitudes can be observed mainly in 0–0.4 Hz. The RMSE of the system under this excitation is 0.64 mm, and Figure 10 shows that the error is mainly concentrated in 0–0.2 Hz.

Figure 11 shows the comparison of the displacements obtained by the proposed system and LDM with the excitation mainly in the high-frequency range. The frequency components with large amplitudes are observed mainly in the range 2.0–2.5 Hz. The RMSE at this excitation is 0.61 mm. Figure 11 indicates that the error is mainly concentrated in the range 0–1.0 Hz.

Figure 12 shows the case when the amplitude of the low frequency is larger. In this situation, the RMSE of the system under this excitation is 0.35 mm. We can see that the error is small among the measured frequency range in this case.

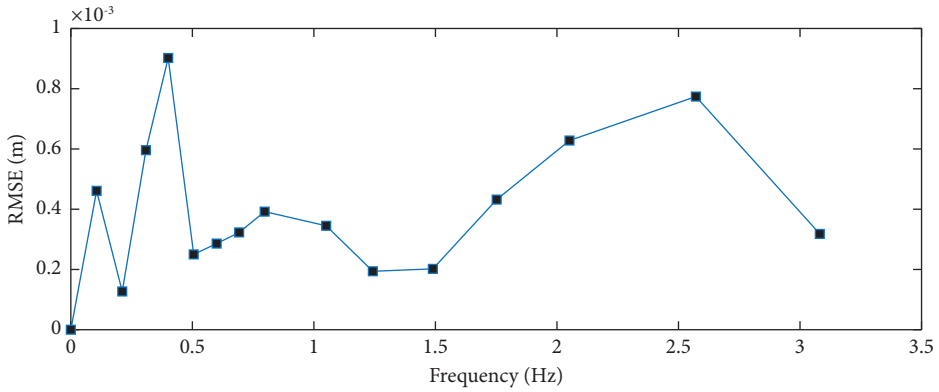


Figure 9: RMSE at different frequencies.

Table 2: Settings of nonharmonic displacement excitation test conditions.

| Case | Details |
|---|---|
| A | Excitation occurs mainly in low frequency |
| B | Excitation occurs mainly in high frequency |
| C | Excitation frequency includes low frequency (<0.4 Hz) and high frequency (>0.4 Hz), and displacement excitation amplitude of low frequency is larger |
| D | Excitation frequency includes low frequency (<0.4 Hz) and high frequency (>0.4 Hz), and displacement excitation amplitude of the high frequency is larger |

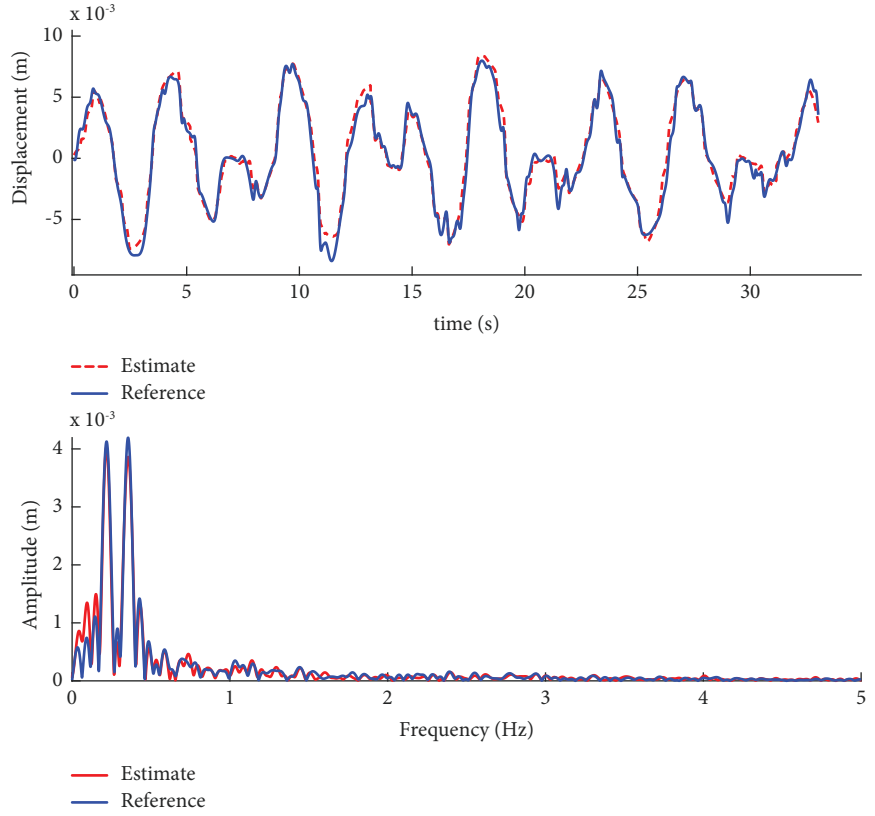


Figure 10: Absolute displacement and spectrum of experimental case A.

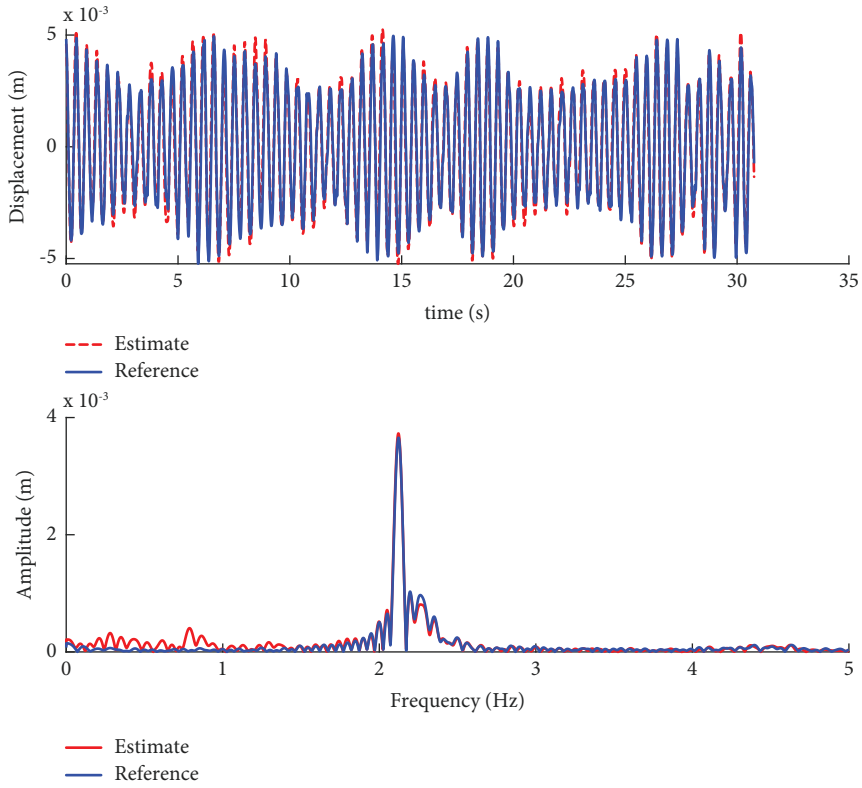


Figure 11: Absolute displacement and spectrum of experimental case B.

Figure 13 illustrates the case with larger high frequency amplitude. In this situation, the RMSE of the system under this excitation is 0.55 mm.

*4.3. Impact Excitation.* Figure 14 compares the displacement measurement results of the proposed system with the LDM under impact loads. The RSME of this displacement measurement system is 0.54 mm.

Table 3 contains the comparison of the RMSE of different cases and displacement reconstruction methods. The proposed method is introduced in Section 3. The method for DHLS is introduced in Section 2. The acceleration estimation involves a baseline correction algorithm with three steps: (1) fitting the baseline of acceleration by the least squares, (2) filtering the acceleration to remove the remaining errors and noise with a high-pass filter, and (3) decreasing the initial values in velocity on the first integration result [21, 22].

Table 3 shows that the RMSE of III (case C) is the lowest, which means the system has higher measurement accuracy with larger amplitudes at low frequency. Furthermore, the proposed system exhibits a lower RMSE than other methods, indicating higher measurement accuracy for each experiment.

We conclude that the system achieves continuous measurement and is also suitable for impact displacement.

## 5. Field Test

To assess the performance of the displacement measurement system and algorithm, a T-shaped rigid frame bridge with a span of 36 m was selected for the field test. The field test was conducted to measure the midspan deflection.

*5.1. Device for Field Test.* We mounted one liquid container of the measurement system at the midspan (moving end). The displacement at the pier position is assumed to be sufficiently small to omit, therefore another container was installed at the pier position (fixed end). Figure 15 shows the bridge condition and location of the sensors.

The main environmental condition affecting the measurements is the temperature. The system also employs image recognition, such that lighting must also be considered at night. The temperature affects the water volume, changing the water level in the tube. The level sensor measures the difference between the two water levels. As the water levels of the two ends from temperature change simultaneously, the measured water level difference remains unaffected by the temperature change. A LED light tape was placed to illuminate the tubes and enable measurement of the water level at night (Figure 15(e)).

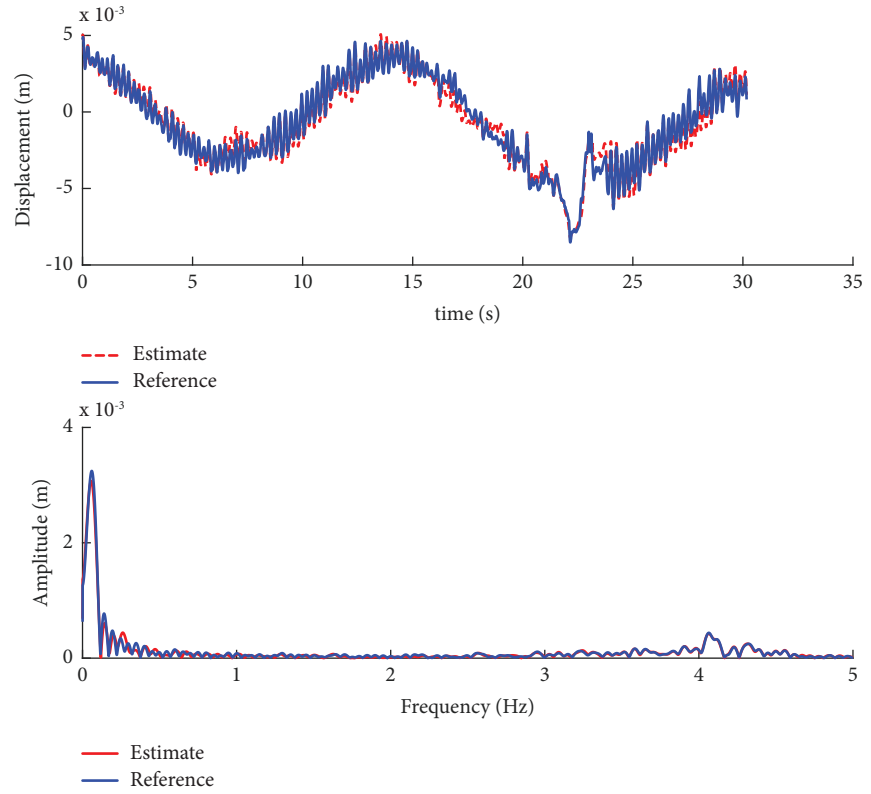


Figure 12: Absolute displacement and spectrum of experimental case C (amplitude of low frequency is larger).

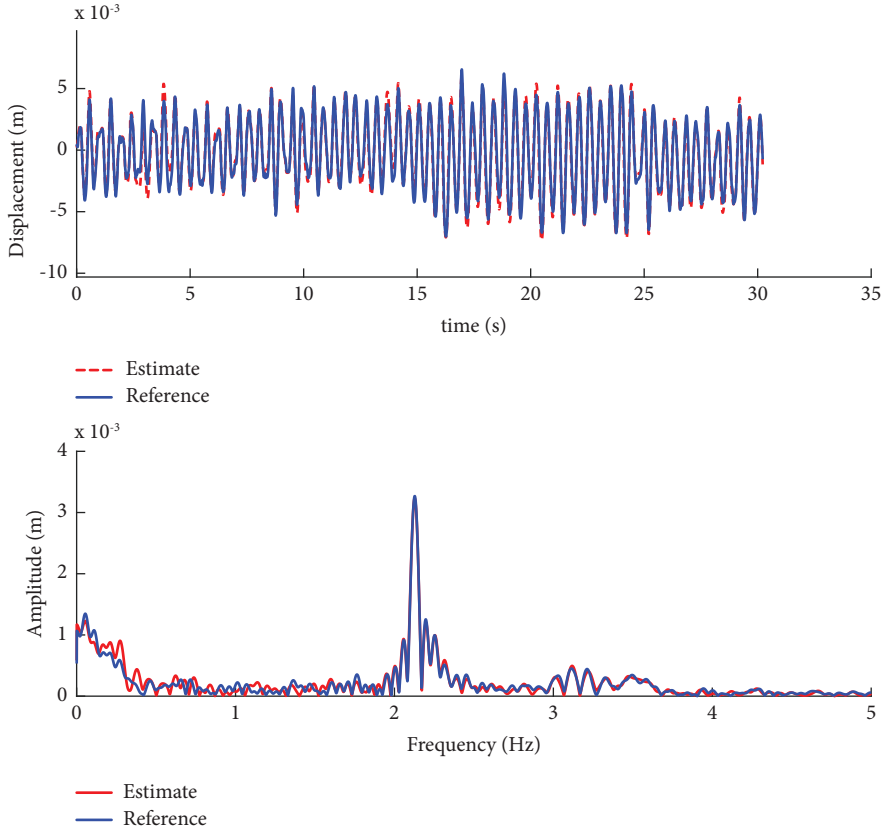


Figure 13: Absolute displacement and spectrum of experimental case D (amplitude of high frequency is larger).

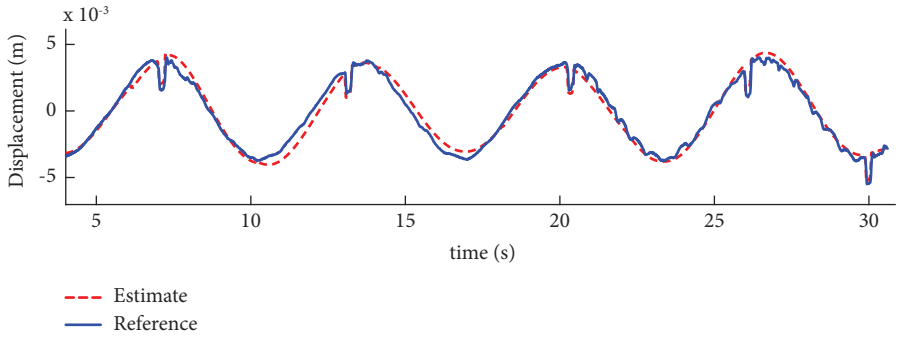


Figure 14: Absolute displacement of experimental condition under impact excitation.

Table 3: Summary of RMSE (mm) for different methods and cases.

| | I | II | III | IV | V |
|---|---|---|---|---|---|
| Proposed system | 0.64 | 0.61 | 0.35 | 0.55 | 0.54 |
| Acceleration estimation | 4.53 | 3.57 | 2.98 | 3.28 | 2.44 |
| DHLS | 3.19 | 2.59 | 5.74 | 2.85 | 0.76 |

I–IV correspond to case A–D in nonharmonic excitation; *V* presents impact excitation.

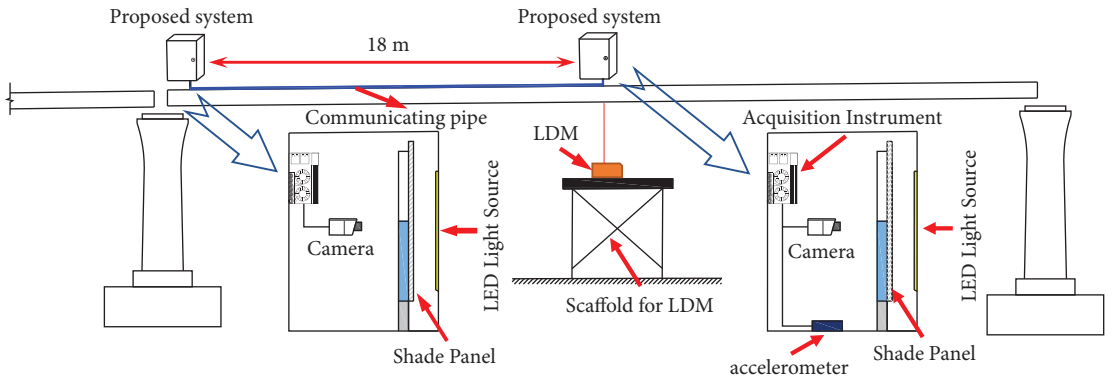


(a)

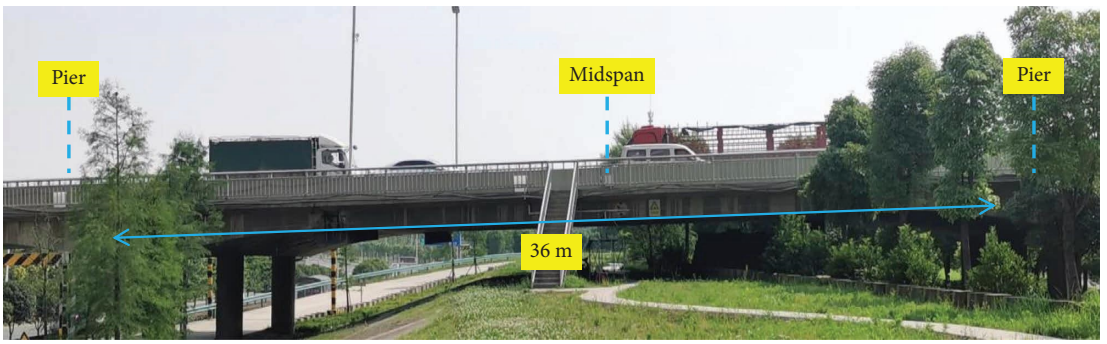


(b)

Figure 15: Continued.

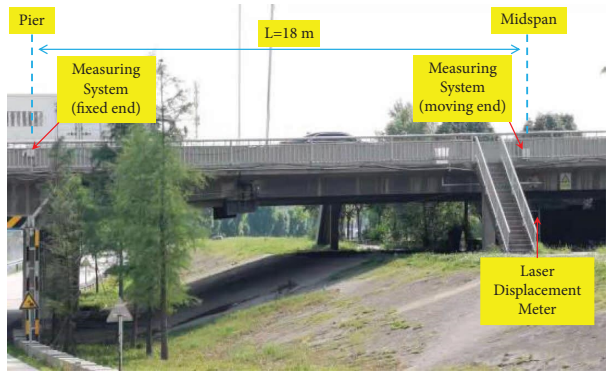


(c)

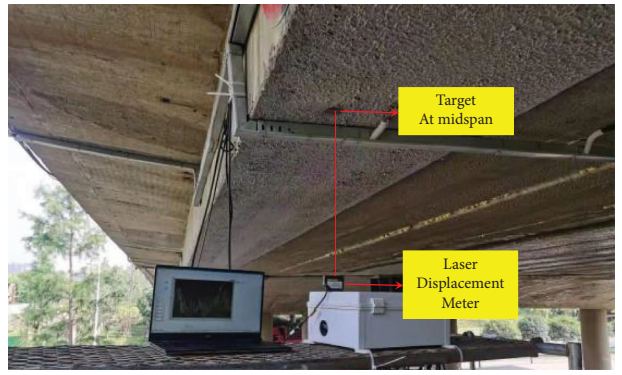


(d)

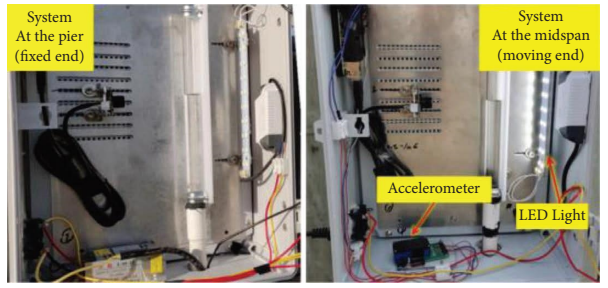


(e)

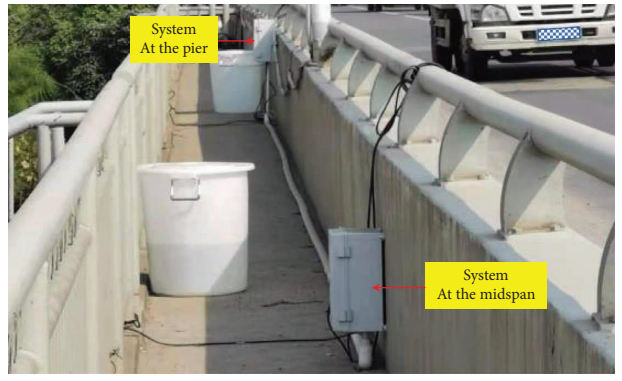


(f)

FIGURE 15: Configurations of measurement systems during the field test: (a) drawing of the test device in the field, (b) field-test bridge, (c) location of each sensor, (d) LDM and target under the bridge at the midspan, (e) construction of proposed system, and (f) system installation location on the bridge.

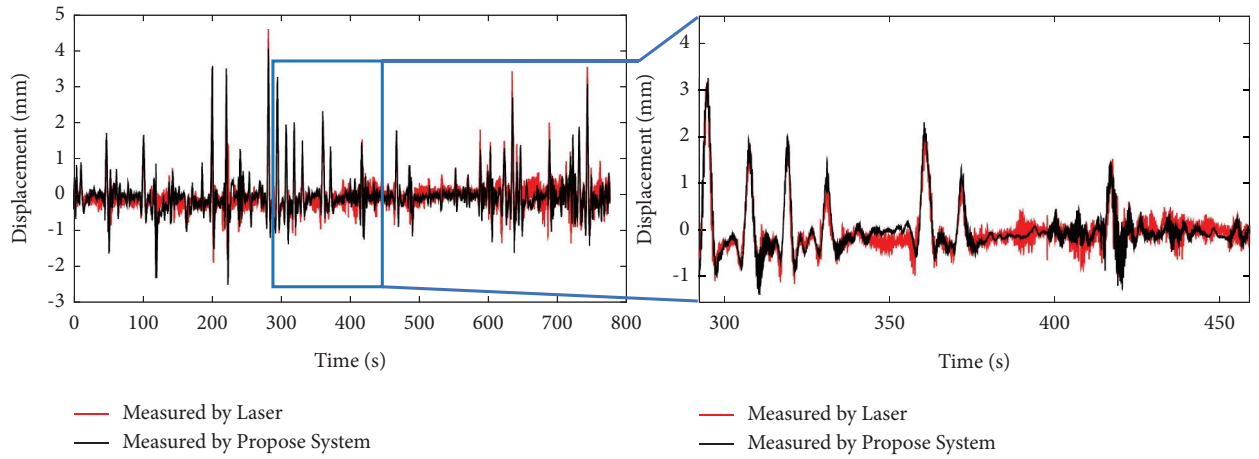


Figure 16: Absolute displacement using proposed approach in field test.

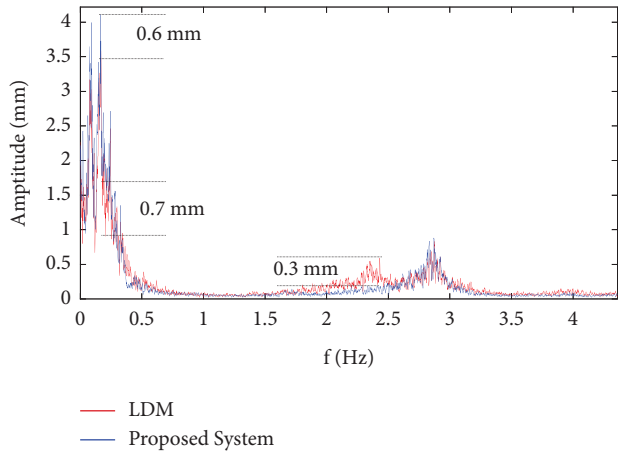


Figure 17: Spectrogram of displacement component of measured data.

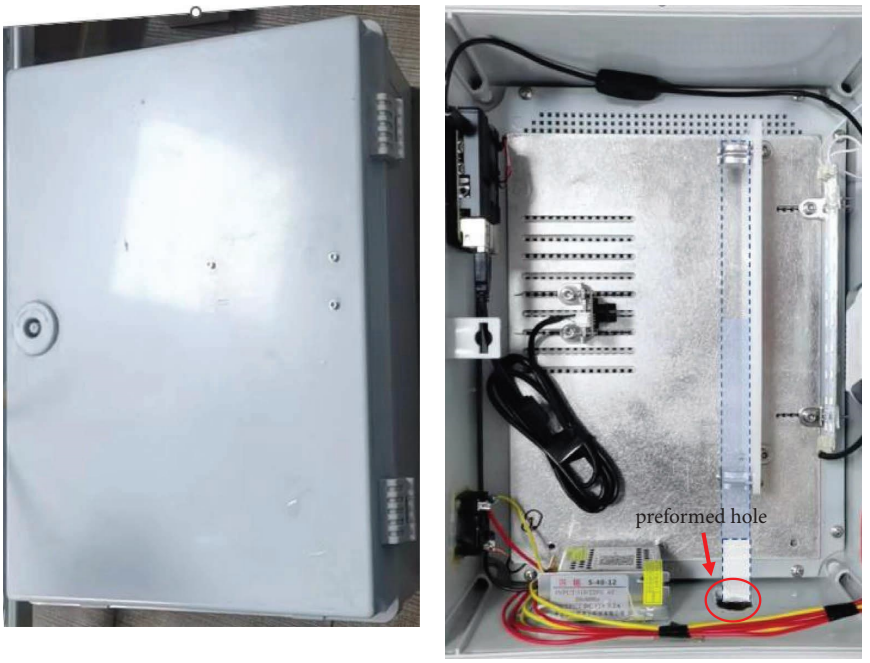


(a) (b)

Figure 18: (a) Dustproof and waterproof box and (b) the components arranged in the box in advance.

*5.2. Results of the Field Test.* Traffic was not blocked on the bridge during the whole test process, and vehicles could pass freely. An LDM was also arranged at the midspan position under the bridge to measure the absolute displacement. The confirmation measurement lasted for ten minutes. We verified the accuracy of the proposed system by comparing the measurement data with the LDM.

We considered 13 min of displacement data measured by the LDM and the proposed system, shown in Figure 16. In order to show the details, we ploted the measured data range 300–450 s in another window. The large waveforms are the deformation caused by vehicles passing the bridge and small waveforms are the high-frequency vibrations associated with the modal frequency of the bridge. The big waveforms are basically the same between proposed system and laser (LDM), but there are errors in small waves. Furthermore, we determined the source of measurement error through spectral analysis. Herein, the RMSE of the proposed system is 0.46 mm. Figure 17 shows the spectrogram of the displacement component measured by LDM and the proposed system. The maximum error is 0.6-0.7 mm, mainly caused by the DHLS measurement error, in the frequency range below 0.4 Hz. We further observe that at approximately 2.5 Hz, there is a maximum error of 0.3 mm, caused by the LDM measurement error (as there is a traffic lane under the field-test bridge, and the passing vehicles vibrate the bracket where LDM is installed).

*5.3. Practicality of the System.* The camera and accelerometer used in the system are industrial-grade products with good durability. The camera can work in the temperature range of −10–65°C, and the accelerometer is in the range of −40–85°C. The system is arranged in a box with dustproof and waterproof functions (shown in Figure 18(a)), which makes the sensor suitable for working in field conditions.

The entire measurement system in the box can be premanufactured at the factory. The communicating pipe is needed to be linked to the box through the predrilled holes (shown in Figure 18(b)) when the system is installed on the bridge. The whole installation process is convenient and expeditious. After installation, the door of the box is closed to protect the measuring system.

While completing the new system, the cost issue was also considered. Since price of the system is very limited (less than $100 when purchased in China), the cost for maintenance and replacement of system is acceptable for practical application.

## 6. Conclusions

This study provides a reference point-free dynamic deflection measurement system for bridges. The proposed system is composed of a DHLS and an accelerometer, and the absolute displacement is reconstructed by fusing the two signals.

The results of this study are listed as follows:

(1) The correction method for DHLS based on the level forced oscillation equation is proposed. The DHLS performance is tested in the laboratory, obtaining a RMSE below 0.41 mm.

(2) The signal fusion algorithm mainly consists of the following steps: Step 1: Displacement reconstruction equation composed of measured acceleration and initial motion conditions; Step 2: Subtraction of the liquid level measured displacement from the reconstructed displacement and obtaining the residual; Step 3: Obtaining the initial state of motion under the condition of minimum displacement residual; and Step 4: Substituting the initial state into the equation to obtain the reconstruction displacement. The experiment result demonstrates that the fusion algorithm improves the adaptation and reduces the displacement drift caused by the acceleration integral.

(3) The field test shows that the proposed system achieves continuous high-precision deflection measurement. Furthermore, the system can be optimized by improving the measurement accuracy of DHLS, which is the main contributor to deflection reconstruction errors.

## Data Availability

No underlying data were collected or produced in this study.

## Conflicts of Interest

The authors declare that they have no conflicts of interest.

## Authors' Contributions

Zhibin Jin conceptualized the study, proposed methodology, wrote the original draft, and was responsible for funding acquisition. Hongda Xia wrote the original draft, performed formal analysis, and designed and completed the experiments. Wenbo Ni validated the study and performed formal analysis. Haoyuan Yang provided software.

## Acknowledgments

This study was supported by the Science & Technology Department of Sichuan Province (Grant no. 2016HH0036), the National Natural Science Foundation of China (Grant no. 51678490), the National Science Fund for Distinguished Young Scholars (Grant no. 51525804), and China-Indonesia Joint Research Center for High-speed Railway Technology (Grant no. KY201801005). The authors would also like to acknowledge Xiaoyan Yang, Xinyu Liu, and Leilei Yao for having supported this study's lab and field tests.

## References

[1] T. Morishita and M. Ikegami, "The slow-ground-motion monitoring based on the hydrostatic leveling system in J-PARC linac," *Nuclear Instruments and Methods in Physics Research Section A: Accelerators, Spectrometers, Detectors and Associated Equipment*, vol. 602, no. 2, pp. 364–371, 2009.

[2] Z. Z. Yin, "Application of hydrostatic leveling system in metro monitoring for construction deep excavation above shield tunnel," *Applied Mechanics and Materials*, vol. 333, 2013.

[3] I. Wyczałek, P. Olaszek, and D. Sala, "Monitoring of the Static and Dynamic Displacements of Railway Bridges with the Use of the Total Station and Set of the Electronic devices," in *Proceedings of the 4th Joint International Symposium on Deformation Monitoring*, pp. 15–17, Athens, Greece, May 2019.

[4] A. A. E. W. Beshr, "Structural deformation monitoring and analysis of highway bridge using accurate geodetic techniques," *Engineering*, vol. 07, no. 08, pp. 488–498, 2015.

[5] R. Lan, Y. Wang, and Q. Chi, "Reconstitution of static deflections of suspension bridge based on inclinometer data IOP conference series earth and environmental science," *IOP Conference Series: Earth and Environmental Science*, vol. 304, no. 3, Article ID 032081, 2019.

[6] H. Sousa, F. Cavadas, A. Henriques, J. Bento, and J. Figueiras, "Bridge deflection evaluation using strain and rotation measurements," *Smart Structures and Systems*, vol. 11, no. 4, pp. 365–386, 2013.

[7] T. Owerko, E. Puniach-Stala, and O. Sukta, "Application of IBIS system to measuring and analysis of displacement on the example of bridge," *Geomatics and Environmental Engineering*, vol. 6, no. 4, p. 61, 2012.

[8] L. H. Zhang, M. Maizuar, P. Mendis, C. Duffield, and R Thompson, "Monitoring the dynamic behaviour of concrete bridges using non-contact sensors (IBIS-S)," *Applied Mechanics and Materials*, vol. 846, pp. 225–230, 2016.

[9] M. Maizuar, E. Lumantarna, M. Sofi et al., "Dynamic behavior of Indonesian bridges using interferometric radar technology," *Electronic Journal of Structural Engineering*, vol. 18, no. 1, pp. 23–29, 2018.

[10] A. Marendić, R. Paar, and I. Grgac, "Monitoring of oscillations and frequency analysis of the railway bridge "Sava" using robotic total station," in *Proceedings of the 3rd Joint International Symposium on Deformation Monitoring (JISDM)*, pp. 1–8, Vienna, Austria, April 2016.

[11] L. Zhang, P. Liu, and X. Yan, "Middle displacement monitoring of medium–small span bridges based on laser technology," *Structural Control and Health Monitoring*, vol. 27, no. 4, Article ID e2509, 2020.

[12] H. H. Nassif, M. Gindy, and J. Davis, "Comparison of laser Doppler vibrometer with contact sensors for monitoring bridge deflection and vibration," *NDT & E International*, vol. 38, no. 3, pp. 213–218, 2005.

[13] J. M. W. Brownjohn, Y. Xu, and D. Hester, "Vision-based bridge deformation monitoring," *Frontiers in Built Environment*, vol. 3, p. 23, 2017.

[14] Y. Xu and J. M. W. Brownjohn, "Review of machine-vision based methodologies for displacement measurement in civil structures," *Journal of Civil Structural Health Monitoring*, vol. 8, no. 1, pp. 91–110, 2018.

[15] Y. Xu, J. Brownjohn, and D. Kong, "A noncontact vision based system for multipoint displacement monitoring in a cable stayed footbridge," *Structural Control and Health Monitoring*, vol. 25, no. 5, p. e2155, 2018.

[16] H. Lee and D. Han, "Deformation measurement of a railroad bridge using a photogrammetric board without control point survey," *Journal of Sensors*, vol. 2018, Article ID 6851252, 10 pages, 2018.

[17] J. Yu, X. Meng, B. Yan, B. Xu, Q. Fan, and Y. Xie, "Global Navigation Satellite System-based positioning technology for structural health monitoring: a review," *Structural Control and Health Monitoring*, vol. 27, no. 1, Article ID e2467, 2020.

[18] H. Yoon, J. Shin, and B. F. Spencer, "Structural displacement measurement using an unmanned aerial system," *Computer-Aided Civil and Infrastructure Engineering*, vol. 33, no. 3, pp. 183–192, 2018.

[19] Y. Liu, Y. Deng, and C. S. Cai, "Deflection monitoring and assessment for a suspension bridge using a connected pipe system: a case study in China," *Structural Control and Health Monitoring*, vol. 22, no. 12, pp. 1408–1425, 2015.

[20] D. Arias-Lara and J. De-la-Colina, "Assessment of methodologies to estimate displacements from measured acceleration records," *Measurement*, vol. 114, pp. 261–273, 2018.

[21] A. Converse and A. Gerald Brady, *BAP Basic strong-motion Accelerogram Processing Software, Version 1.0*, US Department of the Interior, US Geological Survey, Virginia, 1992.

[22] H.-C. Chiu, "Stable baseline correction of digital strong-motion data," *Bulletin of the Seismological Society of America*, vol. 87, no. 4, pp. 932–944, 1997.

[23] Ki-T. Park, S. H. Kim, H. S. Park, and K. W. Lee, "The determination of bridge displacement using measured acceleration," *Engineering Structures*, vol. 27, no. 3, pp. 371–378, 2005.

[24] B. Liu, A. I. Ozdagli, and F. Moreu, "Direct reference free measurement of displacements for railroad bridge management," *Structural Control and Health Monitoring*, vol. 25, no. 10, Article ID e2241, 2018.

[25] A. I. Ozdagli, J. A. Gomez, and F. Moreu, "Real-time reference-free displacement of railroad bridges during train-crossing events," *Journal of Bridge Engineering*, vol. 22, no. 10, Article ID 04017073, 2017.

[26] Y. Xu, J. M. W. Brownjohn, D. Hester, and K. Y. Koo, "Long-span bridges: enhanced data fusion of GPS displacement and deck accelerations," *Engineering Structures*, vol. 147, pp. 639–651, 2017.

[27] S. Cho, J. W. Park, R. P. Palanisamy, and S. H. Sim, "Reference-free displacement estimation of bridges using Kalman filter-based multimetric data fusion," *Journal of Sensors*, vol. 2016, pp. 1–9, Article ID 3791856, 2016.

[28] M. Z. Sarwar and J. W. Park, "Bridge displacement estimation using a co-located acceleration and strain," *Sensors*, vol. 20, no. 4, p. 1109, 2020.

[29] C. Zhang, K. Fukami, and S. Matsui, "Primary hydrokinetics study and experiment on the hydrostatic leveling system," *Equilibrium*, vol. 500, p. 1, 2003.

[30] X. Liu, X. Wang, and W. Ni, "Research on liquid level measurement method of connecting pipe based on machine," *vision[J]*, vol. 44, no. 16, pp. 116–122, 2021.

[31] Z. Jin, B. Huang, and J. Ren, "Reduction of vehicle-induced vibration of railway bridges due to distribution of axle loads through track," *Shock and Vibration*, vol. 2018, Article ID 2431980, 14 pages, 2018.